◆ Human Brain Mapping 34:923–935 (2013) ◆

TECHNICAL REPORT

Electric Field Calculations in Brain Stimulation Based on Finite Elements: An Optimized Processing Pipeline for the Generation and Usage of Accurate Individual Head Models

Mirko Windhoff, Alexander Opitz, and Axel Thielscher*

High-Field Magnetic Resonance Centre, MPI for Biological Cybernetics, Tübingen, Germany

Abstract: The need for realistic electric field calculations in human noninvasive brain stimulation is undisputed to more accurately determine the affected brain areas. However, using numerical techniques such as the finite element method (FEM) is methodologically complex, starting with the creation of accurate head models to the integration of the models in the numerical calculations. These problems substantially limit a more widespread application of numerical methods in brain stimulation up to now. We introduce an optimized processing pipeline allowing for the automatic generation of individualized high-quality head models from magnetic resonance images and their usage in subsequent field calculations based on the FEM. The pipeline starts by extracting the borders between skin, skull, cerebrospinal fluid, gray and white matter. The quality of the resulting surfaces is subsequently improved, allowing for the creation of tetrahedral volume head meshes that can finally be used in the numerical calculations. The pipeline integrates and extends established (and mainly free) software for neuroimaging, computer graphics, and FEM calculations into one easy-to-use solution. We demonstrate the successful usage of the pipeline in six subjects, including field calculations for transcranial magnetic stimulation and transcranial direct current stimulation. The quality of the head volume meshes is validated both in terms of capturing the underlying anatomy and of the well-shapedness of the mesh elements. The latter is crucial to guarantee the numerical robustness of the FEM calculations. The pipeline will be released as open-source, allowing for the first time to perform realistic field calculations at an acceptable methodological complexity and moderate costs. *Hum Brain Mapp 34:923–935, 2013.*

Key words: transcranial magnetic stimulation; transcranial direct current stimulation; electric field calculation; structural magnetic resonance imaging

Additional Supporting Information may be found in the online version of this article.

Contract grant sponsor: Max Planck Society

*Correspondence to: Axel Thielscher, Max Planck Institute for Biological Cybernetics, Spemannstraße 41, D-72076 Tübingen, Germany.

E-mail: axel.thielscher@tuebingen.mpg.de

Received for publication 4 March 2011; Revised 4 July 2011; Accepted 9 September 2011

DOI: 10.1002/hbm.21479

Published online 23 November 2011 in Wiley Online Library (wileyonlinelibrary.com).

INTRODUCTION

Determining the brain regions that are affected by the induced currents is a fundamental problem in transcranial magnetic stimulation (TMS) and transcranial direct current stimulation (tDCS). The complex cortical folding pattern causes an inhomogeneous conductivity distribution in the head and affects the induced electric field or currents in a nontrivial way. Calculations based on simplified head models such as the spherical model therefore only capture the gross features of the field distribution. Recent studies report significant deviations between results from simplified approaches and those determined using more realistic head models [Thielscher et al., 2011; Toschi et al., 2009; Wagner et al., 2009]. Correspondingly, the need for better field calculations in human noninvasive brain stimulation is increasingly recognized, with the ultimate wish to incorporate these calculations into neuronavigation systems to improve the spatial accuracy of stimulation [Rusconi and Bestmann, 2009; Sack et al., 2009; Sparing et al., 2009]. However, this wish is far from the current situation. Here, we report an important step toward this goal by presenting an optimized processing pipeline for the generation and usage of realistic individual head models in field calculations.

At the moment, calculations based on realistic models are hampered by several methodological difficulties spanning from the time-consuming creation of the models from structural magnetic resonance (MR) data to their usage in sometimes complex software solutions for numerical techniques such as the finite element method (FEM). As a consequence, studies on realistic field calculations reported results only for single head models up to now. The additional costs in case commercial software solutions are used might pose a further difficulty.

On the neuroimaging side, several packages such as FreeSurfer (surfer.nmr.mgh.harvard.edu) or BrainVoyager (Brain Innovation, The Netherlands) have been developed that can accurately reconstruct the cortical hemispheres from MR data. Even though difficult, the reconstruction of the skull (itself giving a very low MR signal) is rendered possible by FSL brain extraction tool (BET) [Smith, 2002] with acceptable accuracy using the combination of T1- and T2-weighted images. The resulting triangle surfaces represent a basis for building realistic head models but cannot be used as-is for this task. For example, creating a tetrahedral volume mesh from these surfaces is only possible when they do not have topological and structural defects. However, even these high quality surfaces still contain self-intersections, nearly degenerate triangles with very small or very big angles or nearly overlapping triangles with small angles between their planes. Self-intersections will cause the volume meshing to fail. In addition, well-shaped elements are fundamental for the numerical robustness of methods such as the FEM. The quality of the surface triangles therefore directly determines the quality of the final field calculations. Both problems necessitate the careful and nontrivial preparation of the initial surfaces to make them usable for field calculations.

Here, a processing pipeline is introduced that automatically converts the surfaces from FreeSurfer and FSL into high-quality tetrahedral volume meshes for field calculations based on the FEM. With the exception of MATLAB (MathWorks, Natick, MA), the pipeline is fully based on free software. It starts by removing local defects from the surfaces without affecting the overall geometrical accuracy. It is ensured that the surfaces are free of mutual intersections. After reincorporating the corpus callosum (CC), a tetrahedral volume mesh is built. All steps including the interfacing with FreeSurfer and FSL are combined into a single, easy-to-use script. Manual user interference is possible at dedicated points in the processing pipeline to remove remaining geometrical inaccuracies (if necessary) before building the volume model. Based on the resulting individual head models, field calculations for TMS and tDCS can be performed. The last step is based on a MATLAB toolbox for FEM calculations [GetFEM++; Renard and Pommier, 2010] to allow for an easy postprocessing of the results. A tool for the placement of the TMS coil above a target region of the head model is included. We are currently preparing to release our solution as open source. This will allow researchers using TMS and tDCS for the first time to perform realistic field calculations using individualized head models at an acceptable methodological complexity and moderate costs. The head models described in this article will be released together with the software and might already be sufficient to tackle a range of research questions.

MATERIALS AND METHODS

Subjects

Six healthy subjects (three female; age 25 to 30) were included in the study after they had given written informed consent. None of them had a history of neurological diseases. The study was approved by the local ethics committee of the Medical Faculty of the University of Tübingen.

MR Acquisition

Structural MR images were acquired on a Siemens 3 T TIM Trio scanner (Siemens, Erlangen, Germany) equipped with a 12 channel head coil. Two T1-weighted images were acquired for each subject, one with and one without fat suppression (MPRAGE, 192 sagittal slices, matrix size $= 256 \times 256$, voxel size $= 1$ mm^3, flip angle 9°, TR/TE/TI $= 2{,}300/2.98/1{,}100$ ms without fat suppression, TR/TE/TI $= 2{,}300/4.21/1{,}100$ ms when using selective water excitation for fat suppression). Fat suppression led to weaker signals from the skin and the spongy bone of the skull and helped to improve the anatomical accuracy of the reconstructed border between skull and cerebrospinal fluid (CSF; see section mesh generation below). In addition, two

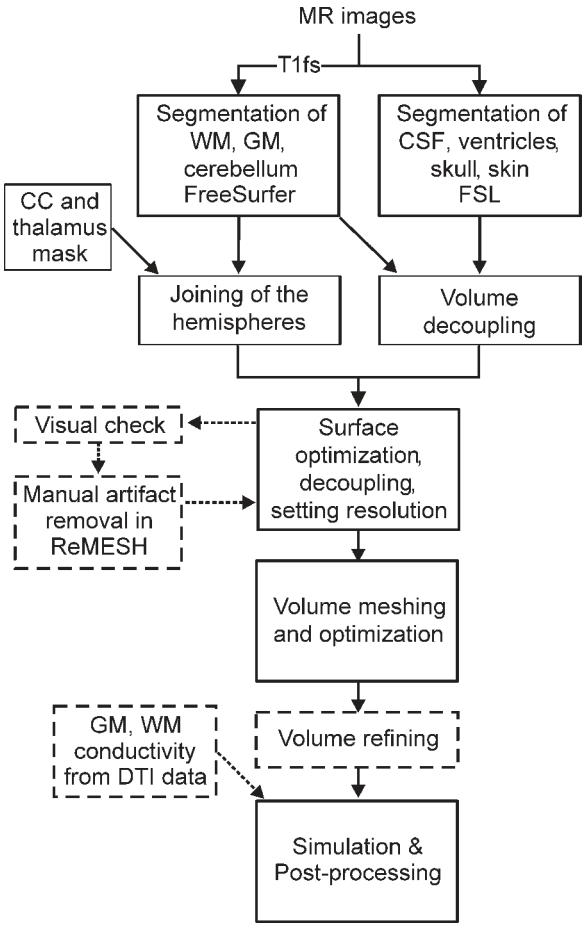

Figure 1.

Overview of the workflow to generate a volume mesh and calculate the electric field induced in brain. Dashed boxes and lines denote optional steps.

T2-weighted images (again with and without fat suppression) were taken (turbo spin echo, 96 sagittal slices, matrix size = 256 × 256, voxel size = 1 × 1 × 2 mm^3, flip angle 110°, TR/TE = 11,990/102 ms, turbo factor 11). In the following, we abbreviate these four images as T1, T1fs, T2, and T2fs. Scanning took ∼ 30 min per subject.

To allow for an estimation of the conductivity anisotropy in white matter (WM) based on diffusion tensor imaging (DTI) data [Tuch et al., 2001], diffusion weighted images were acquired using a twice refocused SE-EPI sequence (72 axial slices, matrix size = 128 × 128, voxel size 1.9 × 1.9 × 2.1 mm^3, TR/TE = 10,500/105 ms, 6/8 phase partial Fourier, GRAPPA acceleration factor 2, seven averages) with 20 diffusion directions and a b-value of 2,000 s/mm^2. Interspersed were seven acquisitions with $b = 0$ s/mm^2.

Overall Workflow

The overall workflow to simulate the electric field of TMS or tDCS consists of three main steps, namely mesh generation, field calculation, and postprocessing (Fig. 1). The initial creation of the volume mesh is the most demanding step and is therefore described comprehensively in the following paragraphs. Shortly, the different tissue regions are segmented from the MR images. Subsequently, surfaces representing the borders between the resulting regions are generated. Also, as the initial segmentation automatically disconnects the two hemispheres, they are joined again by adding the CC. As a key stage in the overall pipeline, the surfaces are then prepared for volume meshing by removing mutual overlaps and self-intersections as well as optimizing the triangle quality. Finally, a tetrahedral volume mesh is generated, and the quality of the tetrahedra is optimized. The mesh generation was originally developed for a combination of normal and fat suppressed MR images and the following description relates to this combination. Importantly, the pipeline can also be used only with the usual images without fat-suppression to reduce the MR acquisition time, leading to a marginally reduced anatomical accuracy of the final head mesh (Fig. S.1B,C in the Supporting Information gives an example). To use the resulting individual head mesh for field calculations based on the FEM, conductivity values are assigned to the different tissue types. At this stage, anisotropic conductivity values for WM and gray matter (GM) derived from DTI data can be included if desired. In case of TMS, the model of the coil is positioned at the desired target location; the magnetic vector potential is determined and used as input for the electric field calculation. In case of tDCS, the anodal and cathodal surface regions are defined and the electric field is determined. Several convenience functions for analysis and visualization of the results are available for postprocessing.

Mesh Generation

An easy-to-use script ("mri2mesh") was created to automatically generate a tetrahedral volume mesh of the head, using the four (or only the two nonfat suppressed) MR images as input. It is fully based on free software and integrates FreeSurfer [Dale et al., 1999; Fischl et al., 1999], FMRIB FSL [Smith et al., 2004], MeshFix [Attene, 2010], and Gmsh [Geuzaine and Remacle, 2009] into a common pipeline for mesh generation. Five tissue types are distinguished, namely WM, GM, CSF (including the lateral ventricles), skull, and skin. The cerebellum and brain stem are incorporated and treated as WM. For a description of the options provided by mri2mesh, see Section A.1 of the Supporting Information.

Segmentation

The segmentation of WM, GM, cerebellum, and brain stem is based on FreeSurfer and uses the fat suppressed T1-weighted image (T1fs) as input. Initial tests revealed that the fat suppressed image gave slightly better results for the GM surface with less anatomical inaccuracies compared with the normal T1-weighted image. FSL BET and

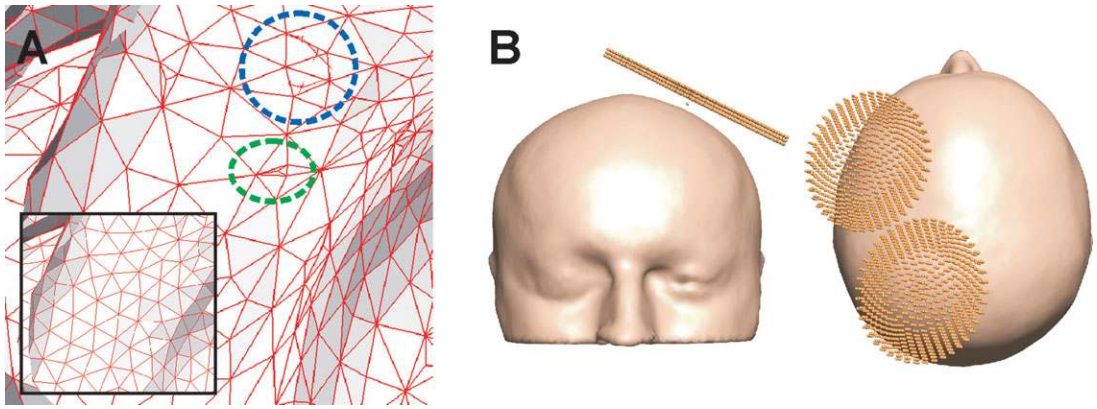

Figure 2.

(**A**) Zoomed view of a triangle mesh (GM surface created by Freesurfer) before the optimization with MeshFix. It contains nearly dihedral triangles (highlighted by the green dashed circle) and intersecting triangles (within the blue dashed circle). The inset shows the same part of the mesh after successful optimization, with the artefacts removed and the overall triangle quality being improved. (**B**) Head with a coil model oriented tangentially to the skin surface over the left motor cortex. The yellow dots indicate the positions of the dipoles modeling the coil. [Color figure can be viewed in the online issue, which is available at wileyonlinelibrary.com.]

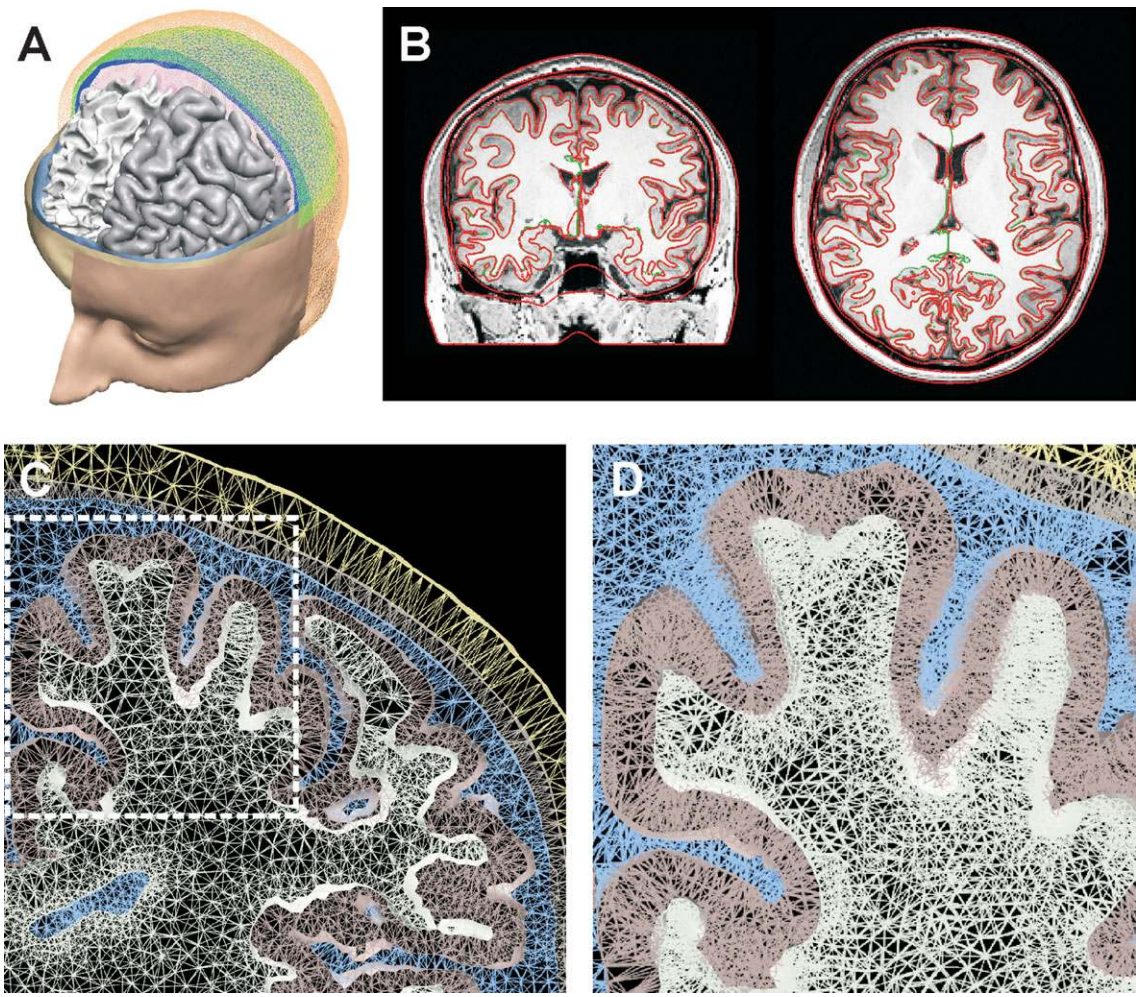

Figure 3.

Meshing results for an exemplary subject (Subject 3). (**A**) Cutaway views of the surfaces of the final meshes. The visible surfaces belong to skin, skull, CSF, GM, and WM. At the back part of the head, the surface edges are displayed. (**B**) Segmented tissue boundaries overlaid onto the anatomical T1-weighted image (coronal and horizontal slices; radiological convention). The red lines denote the final optimized surfaces. In addition, the original FreeSurfer results for WM and GM are shown in green. (**C**) Coronal slice through the left motor cortex showing the tetrahedra of the volume mesh (radiological view). (**D**) Automatic refinement of the volume mesh in a spherical region around the left motor cortex. Shown is a zoomed view of the region highlighted by the dashed white line in C. [Color figure can be viewed in the online issue, which is available at wileyonlinelibrary.com.]

BETSURF are used for the segmentation of the CSF surface and the lateral ventricles. Again, the fat suppressed images (T1fs and T2fs) are used as they give better results for the CSF surface. Segmentation of the skull and the skin is also based on FSL BET and BETSURF, this time using the normal images (T1 and T2) as input.

Decoupling and optimization

The initial surface meshes need to be carefully prepared to make them suitable for subsequent volume meshing. Consequently, the surface processing step represents a key stage in the overall pipeline. It is to large parts based on MeshFix [an open source program for repairing triangle meshes; Attene, 2010] that we extended significantly by custom-written functions. In this step, mutual overlaps and self-intersections are removed, and the triangle quality is enhanced (Fig. 2A). The hemispheres that were artificially cut by FreeSurfer during the segmentation process are joined again by adding the CC. The surface parts close to the midline are modeled in an anatomically more accurate way by adjusting the region around the thalamus. For that purpose, both the masks for the CC and the thalamus (which are assigned to WM later) are taken from the FSL MNI (Montreal Neurological Institute) atlas and transformed into the individual space. Finally, the lateral ventricles are incorporated. The number of triangles used to model the surfaces can be adjusted, enabling the generation of volume meshes of different resolutions.

The decoupling is based on the simplifying assumption that subsequent surfaces are fully contained within each other. That is, the ventricles are fully embedded within WM; WM is completely inside GM; CSF surrounds GM, the brain stem and the cerebellum; the skull contains the CSF and it is completely covered by skin. Although this assumption impairs the anatomical correctness only marginally, it greatly reduces the complexity of the problem to decouple the surfaces of the different materials.

Decoupling is performed pair-wise from inside to outside. In a first pass, the boundaries between the outer tissue layers ranging from GM to skin are decoupled from each other using dilated volume masks and the surfaces are then created based on the resulting, decoupled volumes (using FSL and FreeSurfer routines). This ensures that these outer surfaces that are partly based on different MR images (normal vs. fat-suppressed) and are created by different programs (FSL vs. FreeSurfer) are already separated by a minimum distance of 1 mm before entering the more fine-grained surface processing in the next stage.

Using MeshFix, self-intersections and degenerate or nearly degenerate triangles with very small or large angles are removed from all surfaces. The quality of the triangles is improved by optimizing the spatial uniformity of the distribution of the vertices while preserving the surface shape. In addition, intersections between neighboring surfaces are removed. For example, overlaps between GM and WM are removed by selecting the GM vertices inside the WM surface and pushing them locally outward along the normal direction. As this might create new self-intersections of the GM surface, the described steps are iteratively applied until a stable final result is achieved. Another example to illustrate the methods applied during surface processing is the joining of the hemispheres using the CC. This is done by determining the parts of the CC surface that are inside the WM surfaces and deleting them. Likewise, the parts of the WM surfaces inside the original CC surface are deleted. The surfaces are then joined by inserting new triangles along the resulting gap. To give an overview of all methods used for surface treatment, the features offered by MeshFix are described in detail in Section A.2 of the Supporting Information.

Volume meshing

The optimized surface meshes are used to create subvolumes for the lateral ventricles, WM, GM, cerebellum and brain stem, CSF, skull, and skin. These subvolumes are filled one after another with tetrahedra using Gmsh, and the quality of the tetrahedra is optimized to improve the numerical properties of the mesh [Schöberl, 1997]. Optionally, the tetrahedral resolution in the regions underneath the TMS coil or tDCS electrodes can be selectively enhanced to improve the numerical accuracy of the subsequent FEM calculations (using MATLAB and GetFEM++, see section field calculation and postprocessing below; a corresponding convenience function is provided).

Verification of the results

This optional step of mri2mesh overlays the resulting surface meshes onto the anatomical T1- or T2-weighted image to allow for a visual verification of the anatomical accuracy of the segmentation (e.g., Fig. 3B). In addition, the original surfaces generated by FreeSurfer are displayed to check for putative differences caused by the decoupling and optimization stage. Remaining inaccuracies can be fixed by hand using FreeSurfer or ReMESH [Attene and Falcidieno, 2006; Fig. S.2 gives an example). Afterward, the subsequent processing steps of mri2mesh have to be repeated to create an improved head volume mesh.

Field Calculation and Postprocessing

Conductivity assignment

Five tissue types are distinguished in the resulting volume mesh, namely WM, GM, CSF, skull, and skin. Before the field calculations start, individual conductivity values are assigned to these regions. In this step, the lateral ventricles are treated as CSF and the cerebellum and brain stem as WM. Assuming that the conductivity of the cerebellum equals the one of WM is clearly a simplified approximation. However, in most studies, the lower parts of the brain are not in the focus of the TMS or tDCS and, at the moment, the surface model of the cerebellum is still comparatively coarse. We mainly include it to improve the accuracy of the field calculations in neighboring regions of the cerebrum. If not further specified, standard

conductivity values representing mean values from the literature are assigned to the tissue types [conductivity in [S/m]: WM 0.126; GM 0.276; CSF 1.654; skull 0.010; skin 0.465; Thielscher et al., 2011; Wagner et al., 2004].

Furthermore, anisotropic conductivity values derived from DTI tensors can be included for the GM and WM regions. Custom-written MATLAB functions are provided to convert diffusion to conductivity tensors. Two variations are supported, namely a direct mapping and a "volume normalized mapping." The direct mapping simply scales the DTI tensors to get the conductivity distribution [Rullmann et al., 2009; Tuch et al., 2001]. The volume normalized mapping uses the anisotropy information of the DTI data while maintaining the mean conductivity of the tensors at a predefined value, e.g., at the WM or GM conductivity for the isotropic case [Güllmar et al., 2010]. This approach prevents the problem of very high peak conductivity values that can occur when a direct mapping is used.

The scripts to prepare the DW images for the subsequent estimation of the conductivity tensors are based on the processing steps implemented in the FSL diffusion toolbox [FDT; Smith et al., 2004]. A brain mask is extracted from the first $b = 0$ image and the remaining images are corrected for head movements and distortions caused by eddy-currents using a linear affine coregistration to this first $b = 0$ image. After fitting the diffusion tensors and determining the fractional anisotropy (FA), the FA image is coregistered to the structural T1-weighted image. A two-step procedure is used to account for local distortions in the diffusion weighted images, starting with an affine registration and then applying a nonlinear registration. The resulting warp-field is applied to the DTI data, thereby ensuring that the correct diffusion directions are preserved. Additional functions are provided to convert the DTI tensors into the Gmsh format, so that the accuracy of the coregistration can be visually verified by overlaying the tensors onto the head mesh. As last step, the conversion schemes from the diffusion to conductivity tensors are applied (see Opitz et al., 2011).

TMS

The estimation of the electric field induced by TMS proceeds in three steps, namely positioning of the coil model above the desired target location, calculation of the magnetic vector potential produced by the coil, and the FEM-based calculation of the electric field.

We use magnetic dipoles to model the TMS coils. This allows to easily determine the magnetic vector potential of a coil by summing up the contributions of all the dipoles modeling the coil [Thielscher et al., 2011]. Currently, dipole models for three coil models exist, namely the Magstim 70 mm figure-8 coil, the MagVenture MC-B70, and the Mag&More small eccentric coil. The accuracy of these coil models was verified using field measurements [the mean deviation between the calculated and measured magnetic vector potential was below 4%; Thielscher and Kammer, 2004]. The target coordinates are determined by clicking on the GM surface in Gmsh and the coil model is subsequently automatically positioned 4 mm above the skin (distance is adjustable) and oriented tangentially to the skin surface by means of a custom-written MATLAB function (Fig. 2B).

After positioning the coil model, the magnetic vector potential is determined at each node of the volume mesh and used as input for the FEM-based calculation of the electric field. The FEM is implemented in MATLAB using the GetFEM++ toolbox [Renard and Pommier, 2010].

The electric field induced by TMS is given by $\vec{E} = -\vec{\nabla}\phi - \partial_t \vec{A}$ [Thielscher et al., 2011; Wang and Eisenberg, 1994]. Based on prior literature [Heller and van Hulsteyn, 1992; Wagner et al., 2004], it is assumed that the electric field obeys the quasi-static regime and that displacement currents can be neglected. This simplifies the solution of Maxwell's equations in case of TMS. Using the time derivative of the magnetic vector potential $\vec{A}$ as input, an elliptic differential equation is solved using the FEM to determine the electric scalar potential Φ. Finally, the electric field is calculated by adding the negative spatial gradient of Φ and the negative time derivative of the magnetic vector potential (for details see Section B of the Supporting Information).

TDCS

The electric field generated by tDCS is given by $\vec{E} = -\vec{\nabla}\phi$ [Miranda et al., 2006]. The problem to calculate the electric scalar potential Φ is very similar to the one for TMS. The main difference is that no volume source term occurs (corresponding to the magnetic vector potential at every mesh node in case of TMS), but a Dirichlet boundary condition for the anode and cathode nodes is applied. In doing so, the electric scalar potential Φ is set to predefined values at the skin regions corresponding to the anodal and cathodal electrodes (see Section B of the Supporting Information). At the moment, the electrodes still have to be modeled manually or can be approximated by selecting the underlying nodes of the skin surface instead.

Postprocessing

We wrote several convenience functions for the flexible postprocessing of the results in MATLAB. Besides conversion scripts between the different file formats for the software involved in our pipeline, functions to simplify the extraction of regions or elements, to compare and to merge data were written. As an example, consider the comparison of two simulations using the same volume mesh but with isotropic vs. anisotropic conductivity distributions for WM. After loading the results of the two simulations, the mesh components belonging to WM and GM are extracted (including the data) and the magnitude differences and angular differences of the electric field vectors are determined at each node. Merging the result datasets with the original mesh allows saving a final dataset for viewing with Gmsh.

TABLE I. Surface quality (mean values across subjects) of the WM and GM surfaces as generated by FreeSurfer (before) and after optimization with MeshFix (after)

		WM				GM				GM/WM
		Vertices [$\times 10^3$]	Faces [$\times 10^3$]	Self-int.	Min. angle	Vertices [$\times 10^3$]	Faces [$\times 10^3$]	Self-int.	Min. angle	Mutual int.
Before	Mean	294.2	588.3	**40**	**0**	294.2	588.3	**264**	**0**	**47,602**
	±SD	26.7	53.4	**9**	**0**	26.7	53.4	**66**	**0**	**3,796**
After	Mean	137.8	275.6	0	21.6	135.0	270.1	0	16.2	0
	±SD	0.3	0.5	0	4.5	0.6	1.2	0	0.8	0

Dihedral triangles and (self-) intersections are removed. The resolution is adapted (reduced by a factor 2) and the minimum dihedral angle is increased.

Quality Measurements of the Surface and Volume Meshes

Using the GM and WM surfaces of the six subjects as examples, the surface quality before and after optimization is measured by determining the number of mutual overlaps, self-intersections and the minimum dihedral angle of the triangles. The quality of the tetrahedra of the final volume mesh is determined using three measures (gamma, eta, and rho) provided by Gmsh. All measures are scaled to produce values from 0 (bad quality) to 1 (perfect quality). Values of 1 correspond to a fully regular tetrahedron. Gamma relates the inscribed radius to the circumscribed radius; Eta relates the volume to the surface produced by the edges; Rho is the ratio of the minimum to the maximum edge length. All three measures decrease with growing irregularity of the tetrahedron.

RESULTS

The automatic segmentation and meshing pipeline was successfully tested on the MR data of the six subjects. The final surfaces are shown in Figure 3A and Figure S.1A. Each of the final volume meshes consists $\sim$ 570,000 nodes and 3,300,000 tetrahedra. Figure 3C depicts the volume mesh of Subject 3 in a coronal cut through the left motor cortex as an example. The mesh was exemplarily refined in that region, then consisting of 871,855 nodes and 5,090,432 tetrahedra (Fig. 3D). The creation of one head mesh took about 24 h on an Intel Core 2 Quad CPU at 2.8 GHz, whereof about 22 h were spent for the segmentation with FreeSurfer (all durations were measured using the same PC). As the pipeline is single-threaded, up to four subjects could be processed at the same time without major loss of speed.

Surface and Mesh Quality

The quality of the final volume meshes is determined both by the anatomical accuracy of the segmentation and the quality of the tetrahedra constituting the meshes. Figure 3B shows a slice of the final surfaces (red lines) for Subject 3 overlaid onto the anatomical T1- and T2-weighted images. In addition, the original GM and WM surfaces generated by FreeSurfer are depicted in green. Generally, the reconstructed surfaces closely follow the anatomical borders. The segmentation of the lateral ventricles, WM, GM, and skin is very accurate, while the cerebellum, CSF, and skull in the lower regions of the head are rather coarse approximations. Despite having a lower triangle resolution, the optimized GM and WM surfaces correspond well with the original FreeSurfer surfaces. The hemispheres that were originally separated by FreeSurfer are joined again along the CC. Table I lists the quality for the GM and WM surfaces before and after the optimization (mean values across subjects). The surface decoupling and optimization step succeeds in removing all self-intersections and mutual overlaps while increasing the triangle quality (indexed by the minimum dihedral angle) to a good level. The comparatively many mutual overlaps between the original FreeSurfer surfaces (last column of Table I) mainly occur in the region surrounding the CC (i.e., along the artificial cut), so that most overlaps are removed by inserting the CC and remodeling this region using the thalamus mask. The number of overlaps outside this region is in the range of a few hundreds, i.e., comparable with the number of self-intersections. The quality of the tetrahedra in the volume mesh is documented in Table II using the three quality measures provided by Gmsh (mean values across subjects). Figure 4 shows the corresponding histograms exemplarily for one subject. The overall quality is good, as almost all of the tetrahedra are above 0.25 on each plot. A few tetrahedra are still left that are not very well shaped. However, in all FEM calculations we performed up to now (>100), the convergence behavior was good and thus they appear to be acceptable.

Field Calculations and Postprocessing

Exemplary results of field calculations for TMS and tDCS are depicted in Figures 5 and 6. Figure 5A shows the estimated electric field induced by TMS for typical conductivities, and Figure 5B indicates the estimated

TABLE II. Quality measures Gamma, Eta, Rho and how they are calculated for a tetrahedron (proportional values)

Measure	Proportionality	Mean (mean ± SD)		Min (mean ± SD)		<0.1 in [%] (mean ± SD)	
Gamma	Inscribed radius/circumscribed radius	0.63	0.02	0.002	0.0016	0.04	0.01
Eta	$Volume^{2/3}/sum(edge\ length^2)$	0.77	0.02	0.011	0.0079	0.01	0.01
Rho	Min(edge length)/max(edge length)	0.55	0.02	0.013	0.0101	0.03	0.03

Possible values of these measures range from 0 (bad quality) to 1 (perfect quality). The three rightward columns show the mean and the minimum quality values of the tetrahedra as well as the proportion of tetrahedra having values < 0.1. Listed are mean values and standard deviations (SD) across all six subjects.

difference of the electric field calculated with DTI-derived conductivities for WM and GM. Figure 6 shows the estimated field generated by two (circular) electrodes at typical positions [above the right eye and over the left motor cortex; Nitsche and Paulus, 2000]. Interestingly, inspection of Figure 6B reveals comparatively high field strengths in parts of the CC. Comparison of Figure 6C,D clearly demonstrates that this effect is caused by the lateral ventricles neighboring the WM.

The calculation of the electric field for TMS with a mesh consisting of ~ 3 million tetrahedra took about 1 h and needed less than 4 GB RAM. For the refined version (5 million tetrahedra), it took about 3 h, and the memory consumption was below 6 GB. The values for the tDCS simulations are similar.

DISCUSSION

Realistic field calculations based on accurate individual head models are necessary to better understand the biophysical effects underlying human brain stimulation. However, the generation of the head models is difficult and very time consuming when done manually. For example, in the past, we spent several weeks of mostly manual work to create a single accurate volume mesh [Thielscher et al., 2011]. In contrast, the work presented here allows for a fully automated mesh generation within 24 h. This significant reduction in time and manual effort is key to a more frequent usage of field calculations in brain stimulation, enabling to perform accurate multisubject simulations. Future studies might try to correlate inter-individual differences in the physiological or behavioral effects of brain stimulation with the differences in the induced fields to gain a deeper understanding of the position of the targeted brain areas and the biophysical key factors governing the stimulation effects observed in the experiments. For example, accurate field calculations might help to shed new light on the "classic" finding of interindividual differences in the motor threshold for TMS [a simple measurement of the coil-cortex distance can only account partly for the observed variance; Kloppel et al., 2008; McConnell et al., 2001; Stokes et al., 2007]. In a similar vein, individualized field calculations might contribute to a better understanding of the origin of the "anisotropy" of motor evoked potentials as observed when rotating the TMS coil [Thielscher et al., 2011].

Summary of Findings and Features

We set up a complete software pipeline for field calculations in brain stimulation, starting with the automated segmentation and mesh generation to the FEM-based simulations. While each of these steps represents a difficult problem on its own, the combination of established and

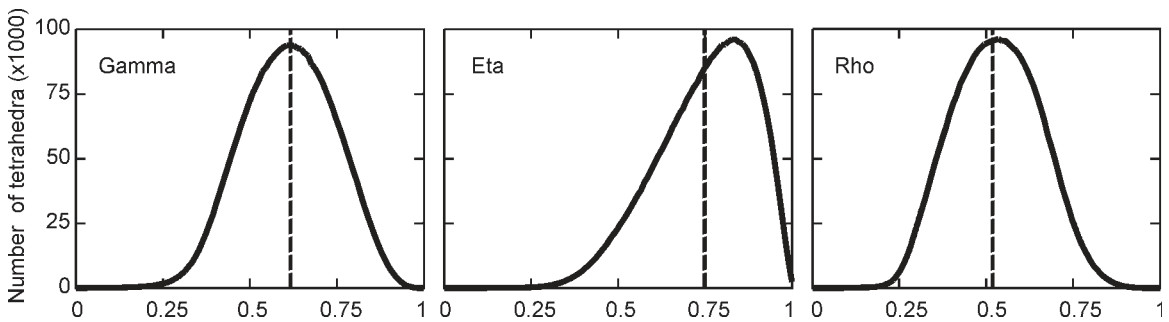

Figure 4.

Quality of the volume mesh for Subject 3, assessed using different quality measures (Gamma, Eta, and Rho; see Table II for a description). The histograms depict the distribution of the tetrahedra across the quality range (0: bad quality; 1: perfect quality). The dashed lines represent mean values.

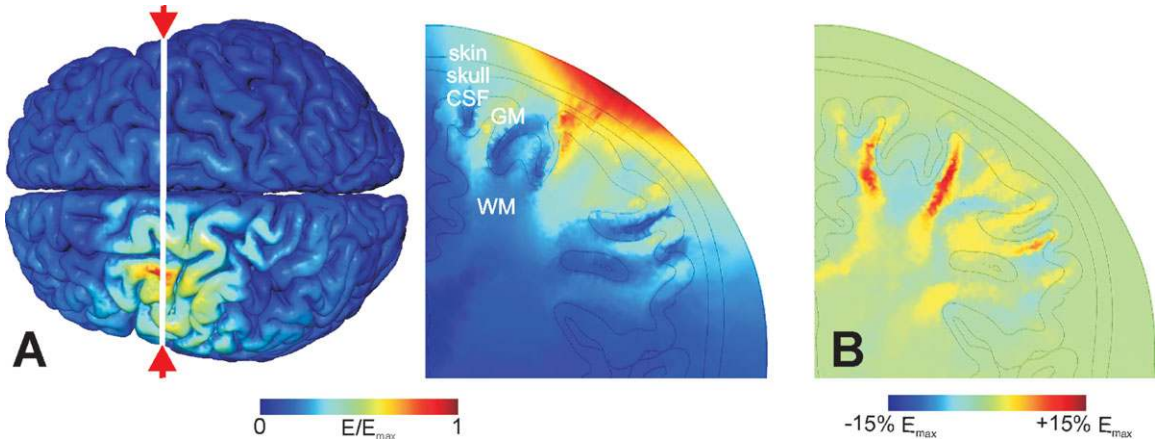

Figure 5.

Exemplary results for the electric field induced by TMS. The coil was positioned over the posterior part of the left middle frontal gyrus of Subject 3, and the coil handle was oriented approximately in direction of the white line. Typical conductivities were used (see section conductivity assignment in Materials and Methods). (**A**) Electric field shown on the GM surface and for a coronal slice as indicated by the white line (radiological convention). (**B**) Exemplary visualization of the difference between the electric fields calculated for anisotropic versus homogeneous GM and WM conductivities. In the anisotropic case, the conductivities were derived from DTI data using a volume constraint mapping, i.e., the mean conductivities were kept identical to the homogeneous case (see section conductivity assignment). This example only serves to demonstrate the possibility to include DTI-derived conductivity estimates in the simulation. A detailed analysis of the results are beyond the scope of this work (please refer to Opitz et al., 2011). [Color figure can be viewed in the online issue, which is available at wileyonlinelibrary.com.]

well-tested software packages for neuroimaging, computer graphics, and FEM calculations that were extended by custom-written software allowed us to build a coherent and easy-to-use solution. Emphasis was placed on using free software. All tools are supported by vivid communities and are constantly refined, which promises to result in enhanced capabilities of our pipeline in turn. The pipeline was successfully tested on MRI data of six subjects. It performed stably and gave anatomically accurate results and volume meshes of good quality in all cases. Exemplary field calculations performed with the six volume meshes showed good convergence behaviors in all cases (Fig. S.1A depicts the resulting estimated field distributions). The FEM library interfaces with Matlab, in turn allowing for easy postprocessing of the results (at the cost of requiring proprietary software at this step). The pipeline is optimized for field calculations in brain stimulation and provides useful features such as tools for an easy coil placement or an automatic mesh refinement underneath the coil. However, the triangulated surface meshes or tetrahedral volume meshes might be useful for other applications such as electro- (EEG) or magnetoencephalography (MEG) as well.

Alternative Approaches

Given the complexity of the overall problem, many alternative solutions to meshing and numerical field calculations can be pursued. For example, an alternative way to build a volume head mesh from MR images was presented in a recent study on FEM-based EEG/MEG source localization [Güllmar et al., 2010]. In that study, a hexahedral mesh with one hexahedron per voxel was used, allowing for a straight-forward generation of the volume mesh from the MR image. The geometric accuracy was subsequently improved by shifting the nodes at the borders between neighboring tissue classes to smooth the shape of the boundary (thereby producing irregular hexahedra). However, initial tests revealed that high computational resources were needed in our case to calculate the induced field in brain stimulation using hexahedral meshes derived with this approach. This was mainly caused by the homogeneous size of the hexahedra over the whole volume of the head. As a consequence, using a high spatial resolution to accurately model the highly folded gyri and sulci necessarily resulted in a high number of elements. In contrast, the element density scales with the inhomogeneity of the surrounding region in the tetrahedral meshes used in our approach. Furthermore, the possibility to better approximate the tissue boundaries by shifting the nodes of the hexahedra is limited, as ill-shaped hexahedra with extreme angles are to be prevented to allow for FEM calculations. As a consequence, the hexahedral meshes appeared to be geometrically less accurate, when compared with our tetrahedral meshes.

Several approaches have been published to calculate the electric field or currents generated in brain stimulation using numerical methods other than the FEM [Cerri et al., 1995; Salinas et al., 2009; Toschi et al., 2008]. The boundary

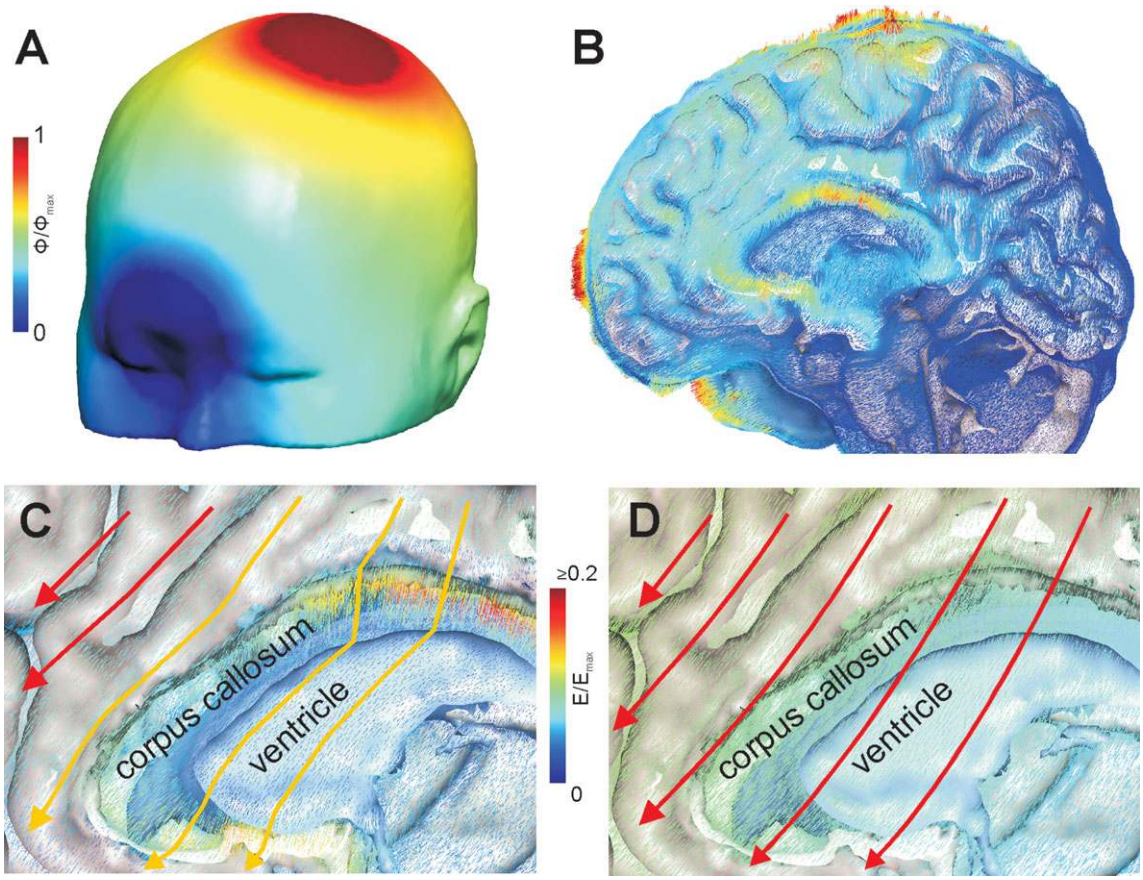

Figure 6.

Exemplary results for the electric field induced by tDCS. The electrodes were positioned above the right eye and the left motor cortex of Subject 1. (**A**) Electric scalar potential on the skin surface. (**B**) Sagittal slice close to the midsagittal plane with the electric field overlaid onto the surfaces of WM, GM, and CSF (the small lines denote the direction of the electric field; skull and skin are not shown; same range of values as used for subfigure **C**). (C) Zoomed view showing GM, the CC, and a ventricle. The arrows indicate the direction of the electric field. The bends of the yellow arrows are caused by the inhomogeneous conductivity, with the electric field in the CC being oriented toward the well-conducting ventricle. To highlight the electric field distribution in the CC region, values exceeding 0.2 are clipped to red. (**D**) Electric field distribution when using the same conductivity for GM, WM, and CSF (all set to 0.126 S/m) to demonstrate the influence of the ventricles on the electric field. [Color figure can be viewed in the online issue, which is available at wileyonlinelibrary.com.]

element method (BEM) used by Salinas et al. [2009] has the advantage that it requires less resources and, in turn, the field calculations can be performed faster than with the FEM. However, it is not possible to account for anisotropic conductivity distributions in the BEM, as necessary when using DTI-derived conductivities for the WM. Though, it is important to note that the surfaces created by our approach would be ideally suited for BEM calculations, as they possess a high quality and are free of mutual intersections. Therefore, using the BEM could be considered for the future to speed up the calculations in case of isotropic conductivity distributions.

The finite difference method (FDM) as used by Cerri et al. [1995] and Toschi et al. [2008] requires a regular grid. As already discussed above, a high spatial resolution is necessary for regular grids or hexahedral meshes to reach a level of detail comparable with that of the tetrahedral meshes presented here. This, in turn, results in a high number of elements, requiring long calculation times and high computational resources. For this reason, we suggest the FEM based on tetrahedral meshes to be better suited for this type of calculation. Apart from being based on the FDM, their approach also differs from the one presented here in the way the conductivity values are assigned to the elements. Rather than using conductivity values that depend on the previously segmented regions, an intensity-based mapping from the T1-weighted MR image is applied based on a polynomial fit [Cerri et al., 1995]. Thus, the conductivity determined for each element is only based on the local intensity of the MR image. Given the

intrinsic noise of MR images and the overlapping intensity distributions of different tissues, we suggest that this local approach might be less robust than the region-based approach used here.

Current Limitations and Future Steps

The accuracy of the estimated electric field depends on the validity of the assumptions that underlie the calculations, the geometrical accuracy of the head and coil models, and the accuracy of the numerical methods used.

Here, it is assumed that the rate of change of the induced currents is slow enough so that the electric field obeys the quasi-static regime and that displacement currents can be neglected. This is easily fulfilled for tDCS but also appears to hold for TMS. The range of permittivity values reported for brain tissue indicates that the ratio between displacement and conduction currents is much smaller than one in the frequency range of TMS pulses ($\sim$ 1–10 kHz). In concordance, both FEM simulations [Wagner et al., 2004] and a theoretical analysis [Heller and van Hulsteyn, 1992] suggest that the electric field is only marginally affected even when assuming permittivity values of $10^4\varepsilon_0$ that are at the upper end of the reported range (ε_0 stands for the permittivity of free space). In Wagner et al. [2004], only very high permittivity values of $10^7\varepsilon_0$ resulted in a clear-cut deviation from the quasi-static limit. However, these permittivity values correspond to non-human muscle tissue [Epstein and Foster, 1983; Hart and Dunfee, 1993]. Accordingly, in vivo measurements in monkey GM demonstrated that the cortical impedance spectrum up to 5 kHz does not depend on frequency [Logothetis et al., 2007].

While the quasi-static limit appears to be justified for TMS and tDCS, some variability exists on the reported conductivity values [see Table 1 in Thielscher et al., 2011]. In Thielscher et al. [2011], we dealt with this uncertainty by demonstrating consistent patterns of electric field distributions for several conductivity schemes including worst-case estimates. Similarly, when using DTI data to estimate the conductivity anisotropy of WM, the mapping between DTI and conductivity tensors is based on a range of assumptions. The basic suggestion is that in structured brain tissue such as WM both the ionic mobility underlying the electrical conductivity and the water mobility underlying DW imaging are similarly restricted by the boundary conditions imposed by the tissue [Tuch et al., 2001]. As a result, both tensors share similar eigenvectors [Basser et al., 1994]. However, the exact relationship between DTI and conductivity tensors is still unclear and several mapping schemes have been proposed in the literature [Güllmar et al., 2010; Rullmann et al., 2009; Tuch et al., 2001]. In Opitz et al. (2011), we therefore tested opposing mapping schemes and demonstrated consistent results across them. However, further experimental studies tackling the conductivity ranges of the different tissues in the head and directly testing the relationship between diffusion and conductivity tensors [Oh et al., 2006] would be clearly beneficial.

The accuracy of the coil models was validated using field measurements [Thielscher and Kammer, 2004]. The geometrical accuracy of the head models is determined by the accuracy of the underlying programs (FreeSurfer and FSL BET) used to create the initial surface reconstructions and was verified by visual inspection. Generally, the segmentation is very good for the upper regions of the head that are normally targeted in brain stimulation. However, some limitations exist for the lower regions. The assumption that the surfaces are completely contained within each other (simplifying the meshing procedure) results in comparatively minor anatomical inaccuracies. For example, each lateral ventricle is modeled as separate volume unconnected to other CSF structures. Therefore, an improvement would be to include the (rather small) third ventricle, which is omitted at the moment. In addition, the CC and the thalamus masks could be taken from the FreeSurfer segmentation instead of the MNI atlas, to better account for the individual shape of these structures. The inclusion of subcortical structures other than the ventricles might be useful in case of tDCS simulations, as well as the automated modeling of the sponges. Finally, the segmentation of the cerebellum is comparatively coarse, e.g., it does not distinguish between cerebellar cortex and WM.

The segmentation of the skull based on the FSL results is rather coarse and done without preserving the facial bones or modeling the eyes. We do not consider this to be a problem for the TMS simulations. The inner skull boundary that mainly determines the direction of the induced fields is accurately modeled in the superficial regions accessible to TMS. However, it might be more important in case of tDCS simulations where distinguishing between spongy and compact bone [Dannhauer et al., 2011] and the inclusion of irregularities such as fissures and foramina might be further important details [Datta et al., 2010].

It should be noted that the FEM is an approximation method. That is, even after model convergence, some differences to the real solution will remain. In Thielscher et al. [2011], the FEM implementation was validated by demonstrating only minor deviations between the FEM results based on linear tetrahedral elements for a multi-shell spherical mesh and the results of an analytical sphere model. In addition, for TMS simulations, the mesh underneath the coil can be selectively refined to improve the numerical accuracy of the solution. In future, selectively refining the regions underneath the tDCS electrodes should help to better approximate the current flow through the skull which represents the main boundary before the currents enter the brain. Even though we did not observe any problems stemming from the few low quality tetrahedra that are still contained in the final volume meshes, one could try to further improve the mesh quality. For example, selectively refining the surfaces in

difficult areas before volume meshing would result in smaller tetrahedra in these regions that would likely also have a better quality.

Accurate estimates of the electric field distribution are only one key component to predict the spatial pattern of the neural effects of TMS or tDCS. The second component is the excitability of the neural elements which depends (among others) on the position, the orientation relative to the induced field, the morphological and electrophysiological properties of the targeted neurons. Until now, most studies neglected these factors and rather made the simplifying assumption that the likelihood to activate a certain brain region directly scales with the locally induced field strength [see Opitz et al., 2011; Thielscher et al., 2011]. However, as started in Salvador et al. [2011], a direct combination of high-resolution FEM simulations with models of the targeted neural elements appears necessary to allow for stronger hypothesis on the neural stimulation effects.

The processing pipeline was not designed to create accurate head models in the presence of pathological conditions. More specifically, its abilities to automatically cope with pathological changes directly depend on the abilities of FreeSurfer to accurately capture the WM and GM surfaces in these cases. Most likely, manual editing of the initial surfaces will be necessary before building the volume head mesh.

The current implementation of the pipeline depends on MATLAB, which is proprietary software. In the future, Scilab (scilab.org) or GNU Octave (www.gnu.org/software/octave/) could be considered as a free alternative to MATLAB. As the FEM library used in the pipeline, GetFEM++, already provides a Scilab interface, porting the calculation routines to Scilab could be achieved with moderate amount of additional work.

However, despite the limitations discussed above, the geometrical accuracy of the resulting meshes is generally high. In addition, to the best of our knowledge, our pipeline is the first integrated, automatic, and easy-to-use processing pipeline for field simulations in human brain stimulation using the FEM. Therefore, it represents an important first step toward more frequent applications of these simulations also in combination with physiological and behavioral studies. Importantly, this will also allow for systematic tests of the validity of the model predictions by, e.g., directly comparing the interindividual variations in the induced field strength with the variations in the physiological or behavioral effect strength. As a next step, we are currently preparing to release the software as open source in the near future (see www.simnibs.org).

ACKNOWLEDGMENTS

The authors thank Heinrich H. Bülthoff for encouragement of this study. The support of Yves Renard when implementing the field equations in GetFEM++ is gratefully acknowledged. Many thanks go to Marco Attene for releasing MeshFix as open source and for his support when extending it.

REFERENCES

Attene M (2010): A lightweight approach to repairing digitized polygon meshes. Visual Comput 26:1393–1406.

Attene M, Falcidieno B (2006): ReMESH: An interactive environment to edit and repair triangle meshes. IEEE International Conference on Shape Modeling and Applications 2006, Matsushima, Japan. pp 271–276.

Basser PJ, Mattiello J, LeBihan D (1994): MR diffusion tensor spectroscopy and imaging. Biophys J 66:259–267.

Cerri G, De Leo R, Moglie F, Schiavoni A (1995): An accurate 3-D model for magnetic stimulation of the brain cortex. J Med Eng Technol 19:7–16.

Dale AM, Fischl B, Sereno MI (1999): Cortical surface-based analysis—I. Segmentation and surface reconstruction. Neuroimage 9:179–194.

Dannhauer M, Lanfer B, Wolters CH, Knosche TR (2011): Modeling of the human skull in EEG source analysis. Hum Brain Mapp 32:1383–1399.

Datta A, Bikson M, Fregni F (2010): Transcranial direct current stimulation in patients with skull defects and skull plates: High-resolution computational FEM study of factors altering cortical current flow. Neuroimage 52:1268–1278.

Epstein BR, Foster KR (1983): Anisotropy in the dielectric properties of skeletal muscle. Med Biol Eng Comput 21:51–55.

Fischl B, Sereno MI, Dale AM (1999): Cortical surface-based analysis—II: Inflation, flattening, and a surface-based coordinate system. Neuroimage 9:195–207.

Geuzaine C, Remacle J-F (2009): Gmsh: A three-dimensional finite element mesh generator with built-in pre- and post-processing facilities. Int J Numer Meth Eng 79:1309–1331.

Güllmar D, Haueisen J, Reichenbach JR (2010): Influence of anisotropic electrical conductivity in white matter tissue on the EEG/MEG forward and inverse solution. A high-resolution whole head simulation study. Neuroimage 51:145–163.

Hart FX, Dunfee WR (1993): In vivo measurement of the low-frequency dielectric spectra of frog skeletal muscle. Phys Med Biol 38:1099–1112.

Heller L, van Hulsteyn DB (1992): Brain stimulation using electromagnetic sources: Theoretical aspects. Biophys J 63:129–138.

Kloppel S, Baumer T, Kroeger J, Koch MA, Buchel C, Munchau A, Siebner HR (2008): The cortical motor threshold reflects microstructural properties of cerebral white matter. Neuroimage 40:1782–1791.

Logothetis NK, Kayser C, Oeltermann A (2007): In vivo measurement of cortical impedance spectrum in monkeys: Implications for signal propagation. Neuron 55:809–823.

McConnell KA, Nahas Z, Shastri A, Lorberbaum JP, Kozel FA, Bohning DE, George MS (2001): The transcranial magnetic stimulation motor threshold depends on the distance from coil to underlying cortex: A replication in healthy adults comparing two methods of assessing the distance to cortex. Biol Psychiatr 49:454–459.

Miranda PC, Lomarev M, Hallett M (2006): Modeling the current distribution during transcranial direct current stimulation. Clin Neurophysiol 117:1623–1629.

Nitsche MA, Paulus W (2000): Excitability changes induced in the human motor cortex by weak transcranial direct current stimulation. J Physiol 527(Pt 3):633–639.

Oh SH, Lee SY, Cho MH, Kim T-S, Kim IH (2006): Electrical conductivity estimation from diffusion tensor and T2: A silk yarn phantom study. ISMRM, Seattle, USA, p.3034.

Opitz A, Windhoff M, Heidemann R, Turner R, Thielscher A: (2011): How the brain tissue shapes the electric field induced by transcranial magnetic stimulation. Neuroimage 58:849–859.

Renard Y, Pommier J (2010): Getfem: A Generic Finite Element Library in C. Documentation, http://home.gna.org/getfem/.

Rullmann M, Anwander A, Dannhauer M, Warfield SK, Duffy FH, Wolters CH (2009): EEG source analysis of epileptiform activity using a 1 mm anisotropic hexahedra finite element head model. Neuroimage 44:399–410.

Rusconi E, Bestmann S (2009): On tickling brains to investigate minds. Cortex 45:1021–1024.

Sack AT, Cohen Kadosh R, Schuhmann T, Moerel M, Walsh V, Goebel R (2009): Optimizing functional accuracy of TMS in cognitive studies: A comparison of methods. J Cogn Neurosci 21:207–221.

Salinas FS, Lancaster JL, Fox PT (2009): 3D modeling of the total electric field induced by transcranial magnetic stimulation using the boundary element method. Phys Med Biol 54:3631–3647.

Salvador R, Silva S, Basser PJ, Miranda PC (2011): Determining which mechanisms lead to activation in the motor cortex: A modeling study of transcranial magnetic stimulation using realistic stimulus waveforms and sulcal geometry. Clin Neurophysiol 122:748–758.

Schöberl J (1997): NETGEN An advancing front 2D/3D-mesh generator based on abstract rules. Comput Visual Sci 1:41–52.

Smith SM (2002): Fast robust automated brain extraction. Hum Brain Mapp 17:143–155.

Smith SM, Jenkinson M, Woolrich MW, Beckmann CF, Behrens TEJ, Johansen-Berg H, Bannister PR, Luca MD, Drobnjak I, Flitney DE, Niazy RK, Saunders J, Vickers J, Zhang Y, Stefano ND, Brady JM, Matthews PM (2004): Advances in functional and structural MR image analysis and implementation as FSL. Neuroimage 23:S208–S219.

Sparing R, Hesse MD, Fink GR (2009): Neuronavigation for transcranial magnetic stimulation (TMS): Where we are and where we are going. Cortex 46:118–120.

Stokes MG, Chambers CD, Gould IC, English T, McNaught E, McDonald O, Mattingley JB (2007): Distance-adjusted motor threshold for transcranial magnetic stimulation. Clin Neurophysiol 118:1617–1625.

Thielscher A, Kammer T (2004): Electric field properties of two commercial figure-8 coils in TMS: Calculation of focality and efficiency. Clin Neurophysiol 115:1697–1708.

Thielscher A, Opitz A, Windhoff M (2011): Impact of the gyral geometry on the electric field induced by transcranial magnetic stimulation. Neuroimage 54:234–243.

Toschi N, Welt T, Guerrisi M, Keck ME (2008): A reconstruction of the conductive phenomena elicited by transcranial magnetic stimulation in heterogeneous brain tissue. Phys Med 24:80–86.

Toschi N, Welt T, Guerrisi M, Keck ME (2009): Transcranial magnetic stimulation in heterogeneous brain tissue: Clinical impact on focality, reproducibility and true sham stimulation. J Psychiatr Res 43:255–264.

Tuch DS, Wedeen VJ, Dale AM, George JS, Belliveau JW (2001): Conductivity tensor mapping of the human brain using diffusion tensor MRI. Proc Natl Acad Sci USA 98:11697–11701.

Wagner T, Rushmore J, Eden U, Valero-Cabre A (2009): Biophysical foundations underlying TMS: Setting the stage for an effective use of neurostimulation in the cognitive neurosciences. Cortex 45:1025–1034.

Wagner TA, Zahn M, Grodzinsky AJ, Pascual-Leone AP (2004): Three-dimensional head model simulation of transcranial magnetic stimulation. IEEE Trans Bio-Med Eng 51:1586–1598.

Wang W, Eisenberg SR (1994): A three-dimensional finite element method for computing magnetically induced currents in tissues. IEEE Trans Magn 30:5015–5023.